Available online at www.sciencedirect.com
ScienceDirect
Journal of Power Sources 179 (2008) 711–722
JOURNAL OF POWER SOURCES
www.elsevier.com/locate/jpowsour

Fluid dynamics performance of different bipolar plates Part II. Flow through the diffusion layer

A. Lozano, L. Valiño, F. Barreras *, R. Mustata

LITEC/CSIC María de Luna 10, 50018 Zaragoza, Spain

Received 15 July 2007; received in revised form 4 December 2007; accepted 24 December 2007
Available online 4 January 2008

Abstract

After studying the velocity and pressure fields inside bipolar plates with different geometries, the analysis has been extended to include the gas passage across the backing or gas diffusion layer (GDL). The gas flow emerging from the porous layer has been monitored using acetone vapor laser-induced fluorescence. The different configurations tested are a parallel commercial case, a set of parallel diagonal channels, a branching cascade-type, and a serpentine distribution of parallel channel blocks. The experimental results have been compared with the predictions obtained from a computational numerical simulation. This study has served to determine the most suitable topology among the tested ones, and has also revealed that knowing the velocity map inside the bipolar plate may not be sufficient to decide if the gas distribution over the catalyst is going to be homogeneous and if a fuel cell is going to operate in an efficient way.

Keywords: PEM fuel cells; Bipolar plate; Fluid mechanics; Flow-field; Visualization; Modeling

1. Introduction

As already discussed in part I of this work [1], a wide variety of bipolar plate topologies are reported in the literature to have been tested in PEM fuel cells to achieve an optimum efficiency [2,3]. Fuel cells are complex electrochemical devices, and reaching the maximum possible efficiency involves a conjunction of different factors. In particular, a high rate of hydrogen decomposition on the anode, and of protons, electrons and oxygen recombination on the cathode are desired. To maintain these electrochemical reactions a stable supply of gases on the catalyst layers is required. If a uniform distribution of the platinum catalyst over either the polymer electrolyte membrane or the gas diffusion layers forming the electrodes is assumed, the reactions that consume the fuel/air can also be expected to be uniform over any given flow path in the plate. If this is the case, the reactant gases should be also uniformly distributed along these flow paths. Commonly, this condition implies a uniform velocity and pressure fields for the flow in the plate, and to obtain them, a correct design of the flow-field geometry of the bipolar plates is needed. On the one hand, a uniform velocity field at the x–y plane guarantees that, as the gases are consumed a constant flow of fresh reactants will reach every zone of the plate. On the other hand, a constant pressure field will contribute to homogeneously distribute the gases over the catalytic electrodes. As demonstrated in a previous research [4], the flow structure inside a bipolar plate can be visualized, and the velocity of reactants determined, applying laser-induced fluorescence in an optically accessible model. Similarly, it has also been proven that the use of numerical simulations can produce accurate results to indicate if both velocity and pressure fields are going to be satisfactory. As a matter of fact, knowing the flow-field inside the bipolar plate might not be sufficient to be sure of the correct performance of the fuel cell. To reach the catalyst the reactants have to flow through the backing layer, also known as gas diffusion layer (GDL), made of a porous and conductor material, most of the times, a carbon paper or carbon cloth with a wet-proofing treatment. However, an apparently right flow behavior in the plate channels can result in a defective pattern after the backing layer, with poor distribution of the gases on the catalyst-covered electrode. Unfortunately, this process is more difficult to be examined experimentally and, when studying gaseous fuels (typically hydrogen) the liquid analogue used in the velocity field anal-

* Corresponding author. Tel.: +34 976 716 440; fax: +34 976 716 456.
E-mail address: felix@litec.csic.es (F. Barreras).

0378-7753/$ – see front matter © 2008 Elsevier B.V. All rights reserved.
doi:10.1016/j.jpowsour.2007.12.095

Nomenclature

Latin letters

a_c	catalyst specific area ($cm^2\ mgPt^{-1}$)
E_C	activation energy for oxygen reduction on Pt ($kJ\ mol^{-1}$)
i	current density ($A\ cm^{-2}$)
j	flux of reactants per unit area ($mol\ s^{-1}\ cm^{-2}$)
K	permeability of porous layer (m)
L_c	catalyst loading ($mgPt\ cm^{-2}$)
nF	charge transferred ($C\ mol^{-1}$)
P, p	pressure (Pa)
R	universal gas constant ($J\ mol^{-1}\ K^{-1}$)
T	temperature (K)
u	velocity of the flow ($m\ s^{-1}$)
V	volume (m^3)
x, y	coordinate system

Greek symbols

β	void part in porous media (m)
γ	pressure coefficient
ε	porosity of GDL
μ	absolute viscosity (Pa s)

Subscripts and superscripts

r	reactant
ref	reference
0	equilibrium

ysis cannot be employed because gas and liquid surface tension are not equivalent and their flow through the porous media will differ.

In the second part of this research, the flow across a diffusion layer located on top of different bipolar plates is examined using acetone vapor planar laser-induced fluorescence. The feasibility of applying this technique to this specific problem has been described in [5]. Here results will be analyzed to compare the performance of the different topologies. Besides, as in part I, it will be demonstrated that a numerical code can accurately reproduce the experimental results, proving that it can be used as a fast and economical design tool.

2. Research methodology

2.1. Experimental technique

The experimental facility used in the present experiments of this research is displayed in Fig. 1. As opposed to the velocity measurements described in part I, in this case, air has been introduced in the plates, with a flow rate of $1.5\,l\,min^{-1}$, which corresponds to flow in excess conditions, discharging to ambient pressure. It is important to discuss the validity and limitations of these experiments to reproduce the gas flow of an operating PEM fuel cell. In this study, the boundary condition behind the GDL (following the flow direction) corresponds to a constant room pressure, where the air is eventually discharged. The gas flow across the GDL is then driven by both diffusion mechanisms and primarily by the pressure gradient, and hence, the tracer concentration is indicative of the pressure field. However, in a working PEM fuel cell the GDL is in contact with a solid boundary, the electrolyte, which acts as a flow drain only through the electrochemical reactions [6].

The rate at which an electrochemical reaction occurs on the electrode surface is equivalent to the rate at which electrons are released (at the anode) or recombined (at the cathode), and can thus be determined by the current generated. Using Faraday's law, the current density defined as the current of ions or electrons

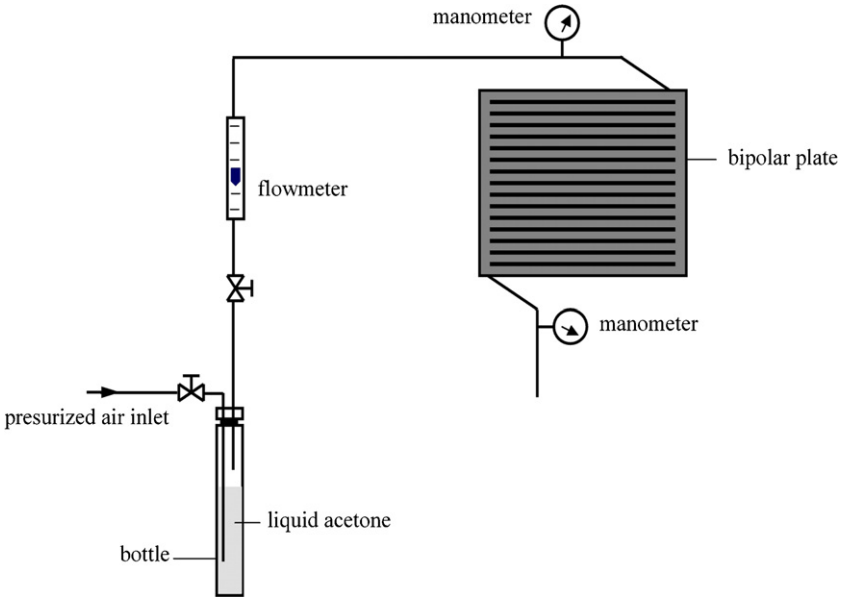

Fig. 1. Experimental facility used for flow visualization after the backing layer.

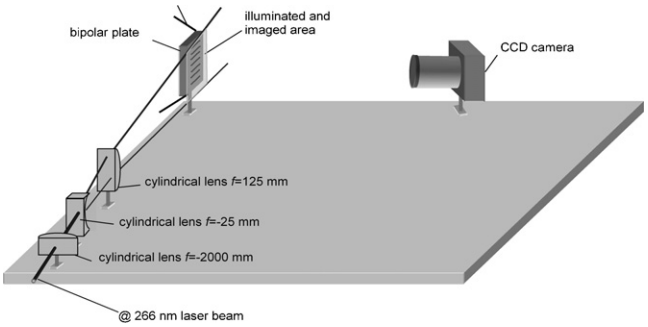

Fig. 2. Optical setup arranged for flow imaging.

per unit area of surface can be expressed as

$$i = nFj, \tag{1}$$

where nF is the charge transferred, and j is the flux of reactants per unit area. The rate at which these reactions take place at equilibrium is called the exchange current density, i_0. The effective exchange current density is dependent on the concentration of reactants, as well as on the temperature, T, and it is also a function of the electrode catalyst loading, L_c, and the catalyst specific surface area, a_c, [7]. Then, the effective exchange current density is given by the equation

$$i_0 = i_0^{\text{ref}} a_c L_c \left(\frac{P_r}{P_r^{\text{ref}}}\right)^{\gamma} \exp\left[-\frac{E_C}{RT}\left(1 - \frac{T}{T^{\text{ref}}}\right)\right], \tag{2}$$

where i_0^{ref} is the exchange current density at a reference temperature and pressure. In this equation γ is the pressure coefficient, E_C the activation energy for oxygen reduction on platinum, and R the universal gas constant. Besides, P_r, T, P_r^{ref}, and T^{ref} are, respectively, the pressure and temperature of the reactants, and the reference pressure and temperature.

When the factors a_c, L_c, γ, E_C, R, T, and T^{ref} are constant, Eq. (2) is reduced to

$$i_0 \propto i_0^{\text{ref}} \left(\frac{P}{P_r^{\text{ref}}}\right)^{\gamma}. \tag{3}$$

Eq. (3) indicates the dependence of the reaction rate on the pressure field. In agreement with this expression, it has been demonstrated both experimentally and numerically that increasing the operating backpressure over the whole electrode area improves the performance of a fuel cell [8]. Accordingly, if a uniform distribution of the platinum catalyst over the electrode is assumed, gas consumption will be proportional to he pressure field. Information of the pressure field in the GDL is, thus, relevant to predict the performance of a fuel cell. Unfortunately, we do not know so far any method to determine

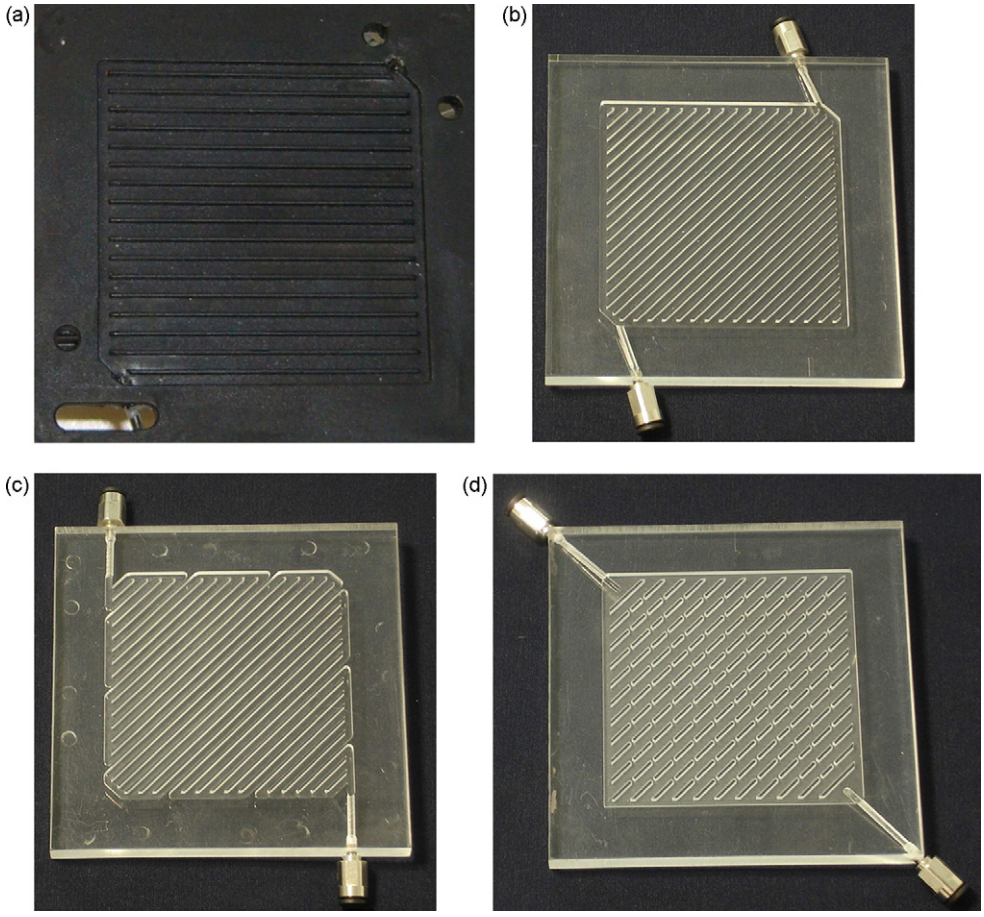

Fig. 3. Pictures of the bipolar plates used in the study: (a) commercial (b) diagonal, (c) parallel-serpentine, and (d) cascade.

the full 2D pressure map on the GDL surface of an operating cell. As an approximation, the experiments here presented can provide indication of this pressure distribution, which in this case is proportional to the marker concentration, if the reaction rate is uniform over the catalytic surface, even when in a real PEM fuel cell there is not a bulk flow across the device.

To visualize the air flow passage across the backing layer, laser-induced fluorescence of acetone vapor has been employed. The use of acetone as a fluorescent tracer in gaseous flows is described in detail in [9]. For completeness, the principal characteristics of this technique will be summarized here. To apply it, a small amount of acetone vapor has to be added to the flow under study. In this case, this has been achieved by bubbling the flowing air inside an acetone bottle. The seeded acetone can be excited illuminating it with UV light. Its absorption peak for transitions to the first excited singlet state is located around 275 nm. Upon excitation, acetone fluoresces in the blue, with a maximum intensity at a wavelength of 435 nm, a decay lifetime of 4 ns and an efficiency of 0.2%. It is interesting to note that the spacing between the absorption and the emission bands enables the possibility to easily filter any possible reflections from the excitation beam.

To excite the tracer, a double cavity Quantel YG781C-10 pulsed Nd:YAG laser has been used, quadrupling the frequency of its fundamental emission to obtain 70 mJ pulses at 266 nm, with a pulse duration of 6 ns. To image the fluorescence emission, an interlined Hamamatsu ORCA-ER 1024 × 1024 pixels CCD camera has been used, placed perpendicular to the bipolar plates. In order to maximize the collected signal the camera has been equipped with a high luminosity lens (Nikon, 50 mm, *f*# 1.2).

The imaged region has been illuminated by a slightly diverging laser sheet, parallel to the bipolar plate, formed by a pair of fused silica cylindrical lenses with focal distances of −25 mm and 125 mm, plus a 2000 mm cylindrical lens to thin the sheet approximately in the middle of the field of view. A sketch of this arrangement is depicted in Fig. 2. To match the resolution of the dye images in the velocity field measurements, the field of view has been adjusted to 72 mm × 72 mm with a spatial resolution of 70.3 μm pixel^{-1}. It is important to take into account that, as a clamped metal frame was used to keep the diffusion layer in place over the bipolar plate, the distance between the laser sheet and the diffusion layer surface was 4.5 mm. As the Schmidt number for the emerging acetone-seeded air flow is about 1.1, at this distance the marker diffusion will act homogenizing the imaged concentration maps.

Temporal sequences have been acquired for the filling process of the bipolar plates with seeded air, starting from an empty initial situation until a stationary state is reached. The time interval between successive images is 0.5 s. It has to be remarked that although for safety considerations and experimental simplicity, air has been used as the working gas, the acetone vapor laser-induced fluorescence technique will work equally with hydrogen or pure oxygen flows.

2.2. Numerical simulations

Numerical simulations to predict the flow behaviour in bipolar plates were presented using a 2D proprietary code in the first part of this work. Essentially, an appropriate 2D version of the Navier–Stokes equations was solved for the different geometries studied.

In the present second part of the paper, the flow through the backing layer is also studied. As indicated in Section 1, the main objective is to observe how homogeneous its arrival to the catalyst layer is. Obviously, this requires a proper prediction of the velocity component perpendicular to the end plane of the GDL, hence perpendicular to the bipolar plate. This is precisely the component of the velocity not considered in the previous part of this work, so it has been necessary to use a full 3D formulation. Besides, the flow is no longer described by the Navier–Stokes equations, but a description of the flow through a porous media, the GDL, is also required, with a physical sound coupling at the interface between the surface of the plate channels and the beginning of the backing layer. A convenient formulation, which does not need any special considerations at the interface (accepting some simplifying assumptions), is given by Ochoa-Tapia and Whitaker [10], and is next described for the present situation.

In the channels of the bipolar plates, the 3D steady version of the incompressible Navier–Stokes equations is used:

$$\text{Continuity}: \quad \frac{\partial u_j}{\partial x_j} = 0, \tag{4}$$

$$\text{Momentum}: \quad u_j \frac{\partial u_i}{\partial x_j} = -\frac{1}{\rho}\frac{\partial p}{\partial x_i} + \mu \frac{\partial^2 u_i}{\partial x_j \partial x_j}. \tag{5}$$

For the GDL, it is convenient to distinguish between two types of volume average of the physical magnitudes of interest

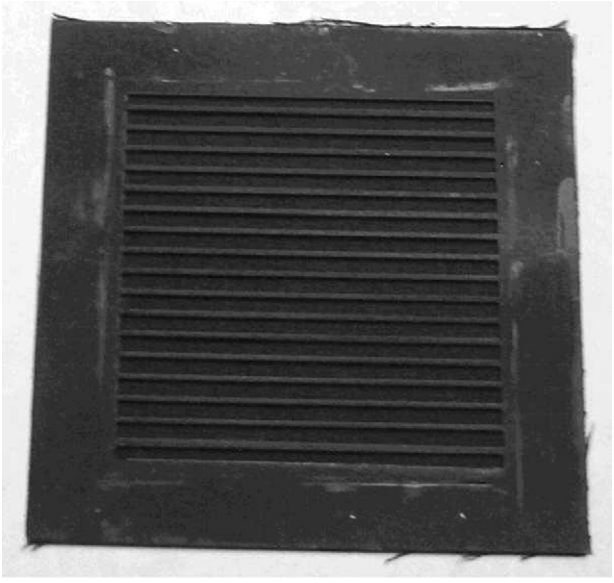

Fig. 4. Image of the metal grid used to hold the carbon cloth in place against the commercial bipolar plate.

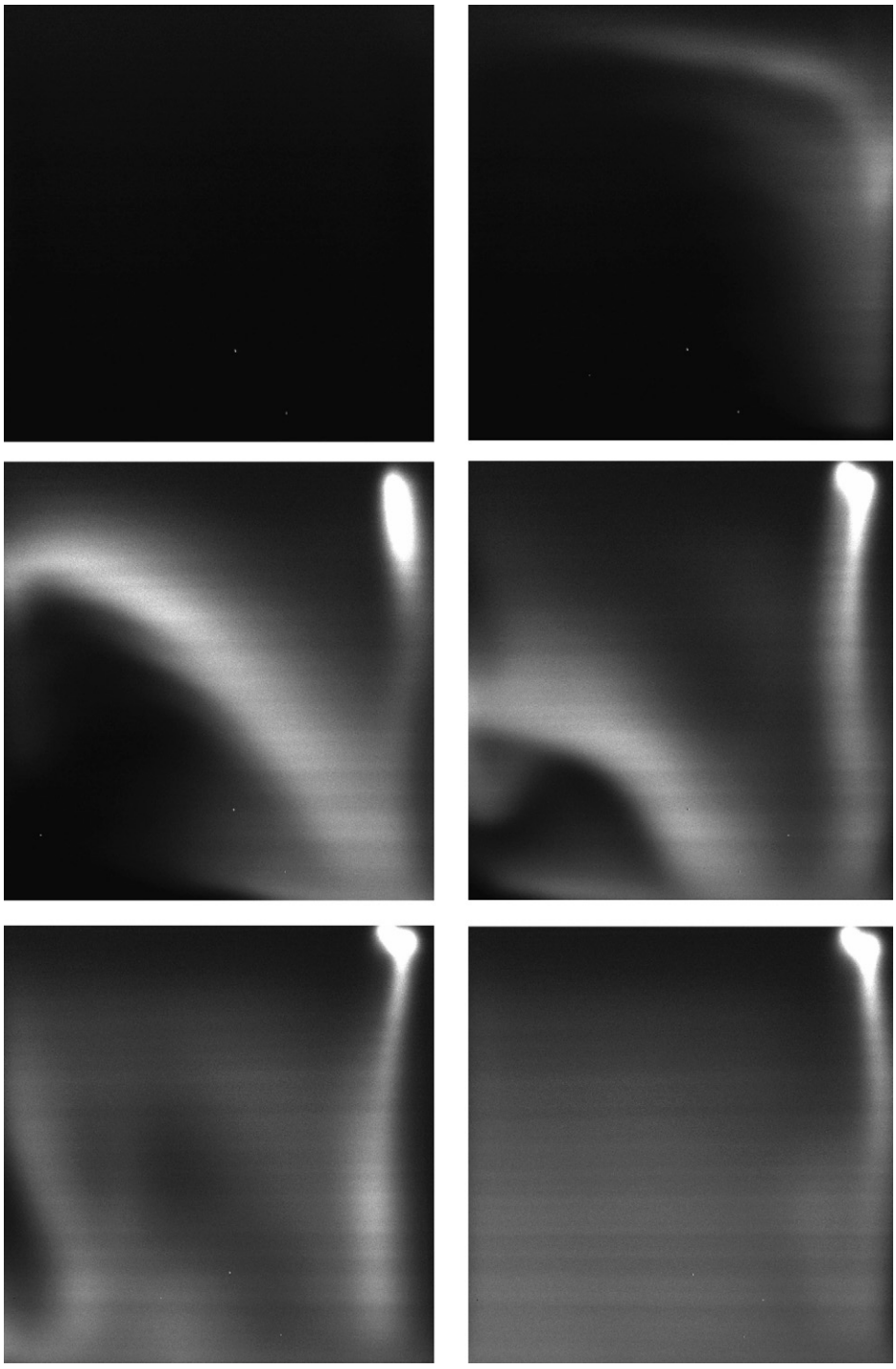

Fig. 5. Temporal sequence showing the flow through the carbon paper when the commercial plate is filled with acetone-seeded air. Images are separated by 0.5 s. Flow rate is 1.5 l min^{-1}.

inside the porous media [10]:

$$\text{Superficial average}: \quad \langle\cdot\rangle = \frac{1}{V}\int_V \cdot \mathrm{d}V, \tag{6}$$

$$\text{Intrinsic average}: \langle\cdot\rangle^\beta = \frac{1}{V_\beta}\int_{V_\beta} \cdot \mathrm{d}V_\beta, \tag{7}$$

where the superscript β (which is not an exponent) indicates the zone available for the fluid inside the porous media (the "void" part in opposition to the solid part), and V indicates a small enough volume used to calculate the average. In agreement with the notation used, V_β indicates the void part inside the volume V, its fraction being the porosity ε by definition. Hence superficial and intrinsic averages are related through $\langle\cdot\rangle = \varepsilon\langle\cdot\rangle^\beta$.

It can be shown [5] that under appropriate conditions, the superficial averaged velocity is the matching quantity to the flow velocity and that the intrinsic averaged pressure is the matching

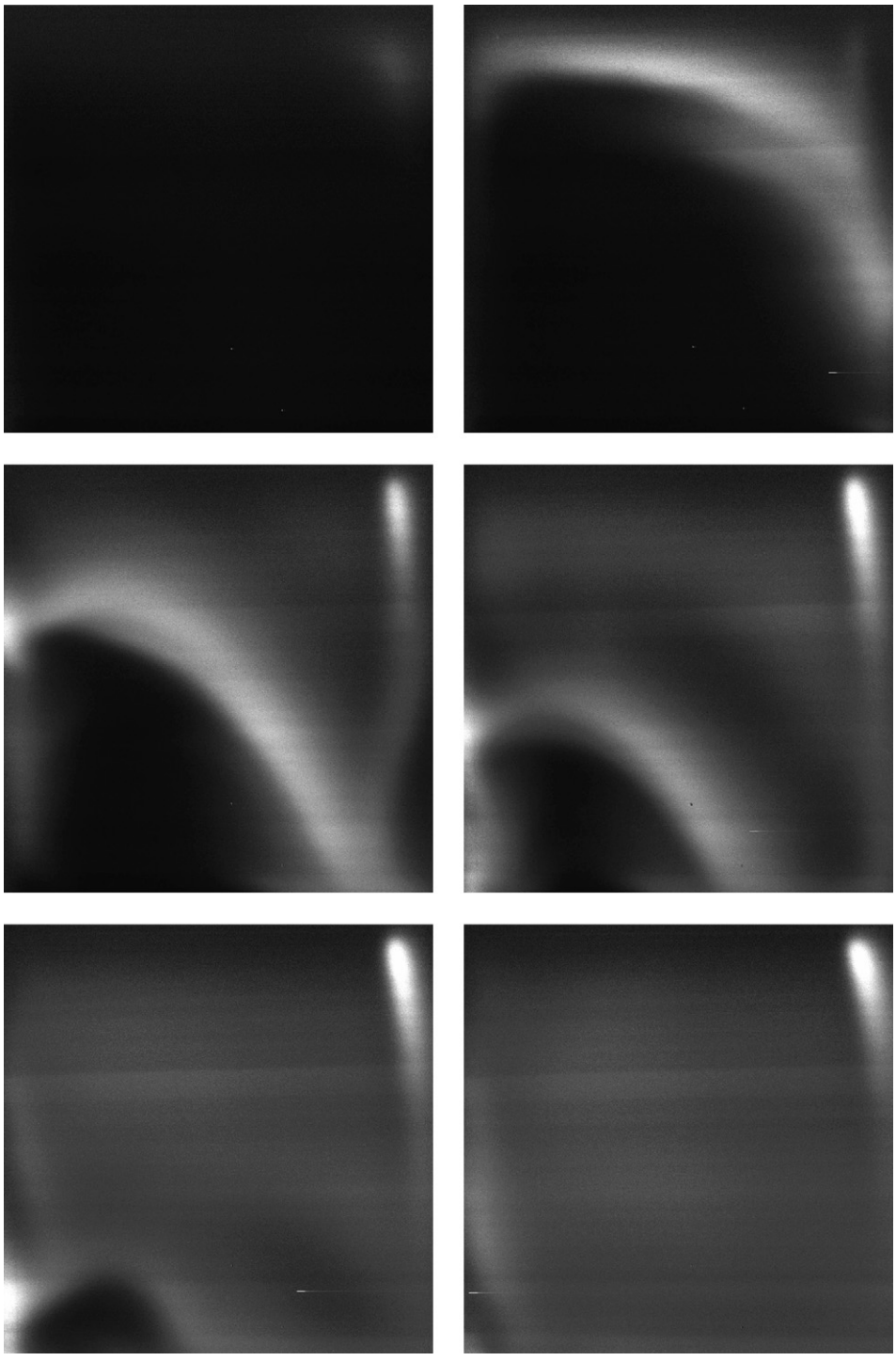

Fig. 6. Same process as in Fig. 5, with the commercial plate covered by a piece of carbon cloth.

quantity to the flow pressure inside the porous media. This is used to simplify the notation, so u and p will be directly written for equations inside the porous media (steady approximation) as:

$$\text{Continuity inside GDL}: \quad \frac{\partial u_j}{\partial x_j} = 0, \tag{8}$$

$$\text{Momentum inside GDL}: \quad \frac{1}{\varepsilon^2} u_j \frac{\partial u_i}{\partial x_j} = -\frac{1}{\rho}\frac{\partial p}{\partial x_i} + \frac{\nu}{\varepsilon}\frac{\partial^2 u_i}{\partial x_j \partial x_j} - \frac{\nu}{K} u_i, \tag{9}$$

where ε is the porosity and K is the permeability, assuming an isotropic and homogeneous porous medium. The second term on

the right-hand-side of Eq. (9) is known as the Brinkman approximation, and the third one reflects the contribution of Darcy's law.

The previous equations have been solved in the geometrical configuration corresponding to the commercial plate (see next section), under the same conditions as those in the experiments, considering a carbon paper GDL. In the present case $K = 8.69 \times 10^{-12}$ m, and $\varepsilon = 0.75$ through the whole porous domain. As mentioned above, the steady state case has been considered.

A finite volume approach using *OpenFOAM*, an open source computational fluid dynamics code, has been followed. Around 200.000 non-uniform hexahedral-like volumes have been needed to properly represent the plate plus the GDL computational domain.

In connection to the discussion in the previous section related to the different boundary conditions on the GDL surface in a real PEM fuel cell and in this model, it has to be noted that the present results can be considered as a preliminary step towards a computer code to simulate the complete device. The boundary condition established as a constant pressure should be replaced in the anode by a modeled gas drain. However, it was considered more interesting to simulate a set of conditions that could be validated comparing with experimental measurements.

2.3. Bipolar plates topologies

As a continuation of the velocity and pressure field analysis, the new measurements have been obtained with the same plate topologies as those in part I. In particular, the plates that were there denoted as diagonal type, serpentine-parallel plate type and cascade flow-field have been tested. It has to be reminded that these geometries were developed after considering the velocity and pressure results that had been obtained in [4] for a commercial plate. Given that the flow across the backing layer was not studied for that case, it has now also been included in the present experiments. Although the detailed geometry of each plate has already been described in the first part of this study, a figure (Fig. 3) is here included depicting all the configurations. In order to perform the experiments, the plates were covered with a 7 cm × 7 cm piece of Toray™ carbon paper. To fix it, both bipolar plate and paper were sandwiched between a back plate and a square frame both made of steel and clamped together. For the commercial plate, some initial tests were performed substituting the paper by an ELAT™ Teflon-covered carbon cloth. Even though the cloth was held by the steel frame, as it is not rigid, the air flow caused it to dome, detaching from the plate ribs and altering the flow pattern in the channels. To avoid this effect, the metal frame was replaced by a metal grid that pressed the cloth against the ribs (see Fig. 4). As will be shown in the next section, the results obtained using the properly fixed cloth and the paper were substantially identical. For this reason, only the carbon paper was chosen as the backing layer in the rest of the experiments, as its rigidity prevented any doming problems.

3. Results

Fig. 5 displays a sequence of images acquired according to the experimental setup sketched in Fig. 2 when the commercial plate covered with a piece of carbon paper is being filled (from an empty initial situation) with air seeded with acetone vapor. It can be observed that the air flow that first emerges from the diffusion layer correlates with the upper and the right lateral channels of the plate, which are also the ones with higher velocities. As time evolves, the emerging flow becomes remarkably uniform, with the exception of a clearly noticeable jet directly exiting from the plate inlet orifice. The intensity of this jet is in part related to the high flow rate and the tilting angle of the inlet channel.

Fig. 6 shows a similar sequence, obtained with the same bipolar plate, but in this case, covered with a piece of carbon cloth fixed with a metal frame as explained in the previous section and depicted in Fig. 4. It is to be noted that the emerging air during the filling process follows a nearly identical pattern to the one presented in Fig. 5. This similitude indicates that the flow behavior is indistinguishable when either carbon paper or cloth are used, and justifies that for the rest of the experiments only paper has been employed.

Results obtained from the numerical simulation study also support the above-commented situations. Fig. 7 shows a 3D cut of the commercial plate showing the pressure distribution (at steady state). Notice the small differences on the pressure values. The largest (although still small) drop in pressure is due to the porous media. Fig. 8 shows the pressure at the surface of the channels. It is observed the effect of the impinging jet at the entrance, as mentioned above when describing Fig. 5. As pressure is the main driving magnitude for the flow in the porous media, it is not surprising that the exit velocity at the end of the GDL (Fig. 9) shows a matching pattern to the pressure field depicted in Fig. 8. The emerging flow becomes rather uniform,

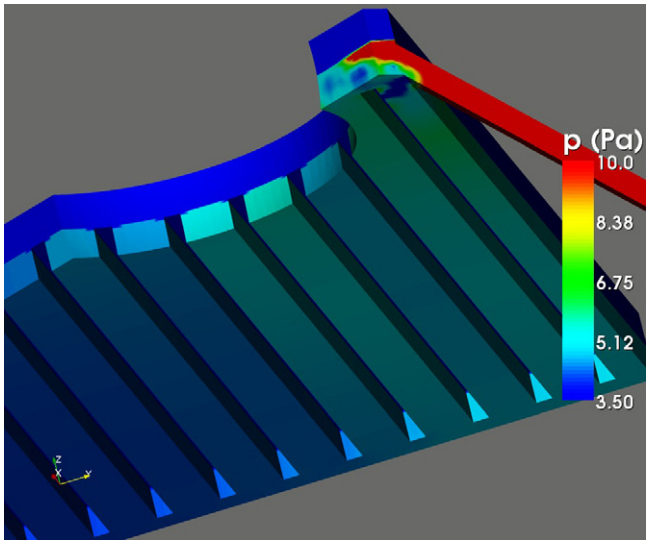

Fig. 7. 3D cut of the commercial plate entrance showing isocontours of pressure. The domain is extended into the air 1.7 mm to compare with experimental data. The view is from the bottom of the plate, and the black lines are the voids where the ribs would be located.

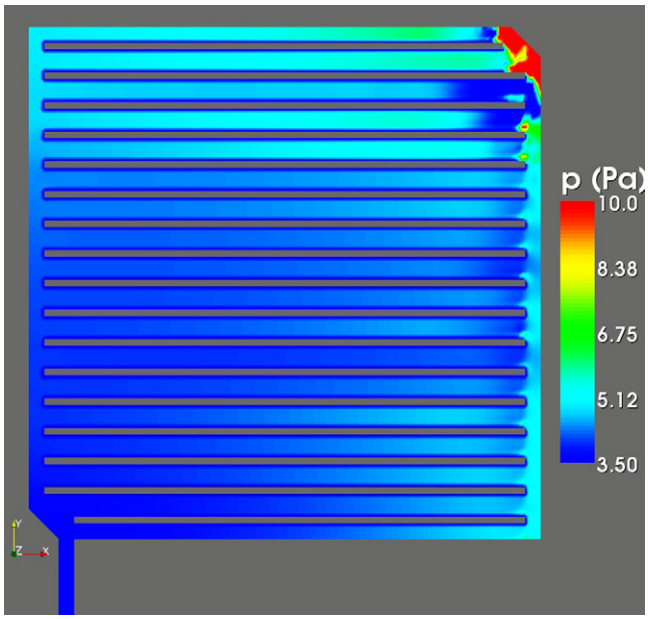

Fig. 8. Pressure values at the surface of the channels of the commercial plate.

with the exception of a clearly noticeable jet directly exiting from the plate inlet orifice. As mentioned in the description of Fig. 5, this increase in pressure is related to the high flow rate and the tilting angle of the inlet channel. The effect of the channel ribs is depicted in the figure as areas of low velocity. It is worthy to indicate that the velocity differences are still meaningful, as yellow areas roughly indicate a double value of that in the green areas. Notice the effect on the right channel and upper channels of the plate. Fig. 10 shows the exit velocity at a plane in the air, some 1.7 mm beyond the GDL end. This location is close to that in the measurements shown in Fig. 5, namely 4.5 mm apart from the backing layer. Observe the good agreement between experiments (the image corresponding to the final state) and numerical simulations. The smearing out effect of diffusion, comparing with results at the GDL exit, is noticeable, and

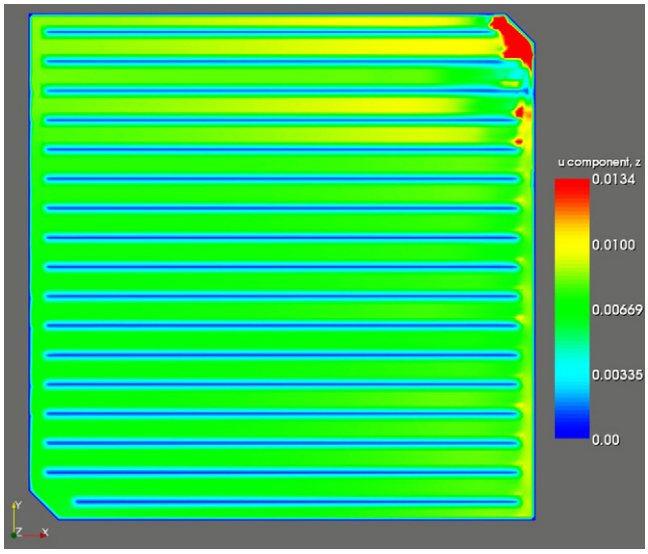

Fig. 9. Normal (z) velocity at the end of the GDL ($m\,s^{-1}$).

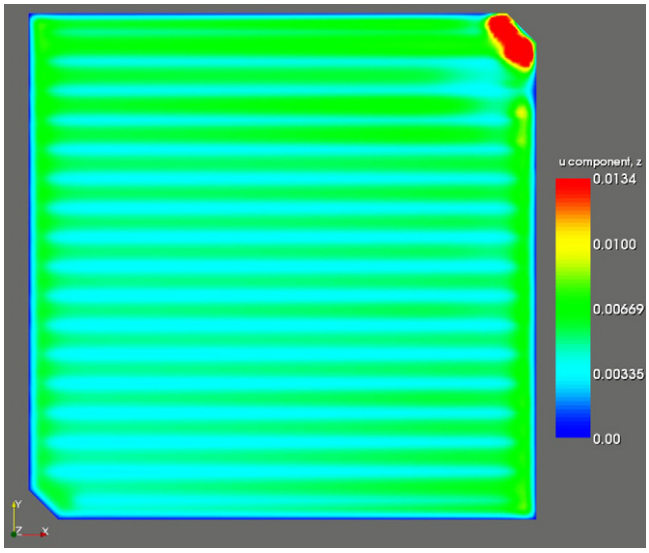

Fig. 10. Normal (z) velocity at the plane of measurement ($m\,s^{-1}$), 1.7 mm in the air.

the effect of the ribs has been partially smoothed out. The longer distance between the imaged plane and the GDL in the experiments can explain why in Fig. 5 the ribs are no longer visible. Fig. 11 depicts the magnitude of the velocity at the middle plane of the plate channels. The pattern reminds the one shown in part I of this research [1]. In most parts of the plate, the velocity component in the direction perpendicular to it is much smaller than in the parallel ones.

The images in Fig. 12 correspond to the experimental visualization of the flow distribution behind the GDL for the serpentine plate. A very homogeneous velocity field had been measured for this topology, but with large maximum pressure values, roughly 2.5 times higher than those obtained for the other bipolar plates, and a significant pressure loss. These effects are reflected in

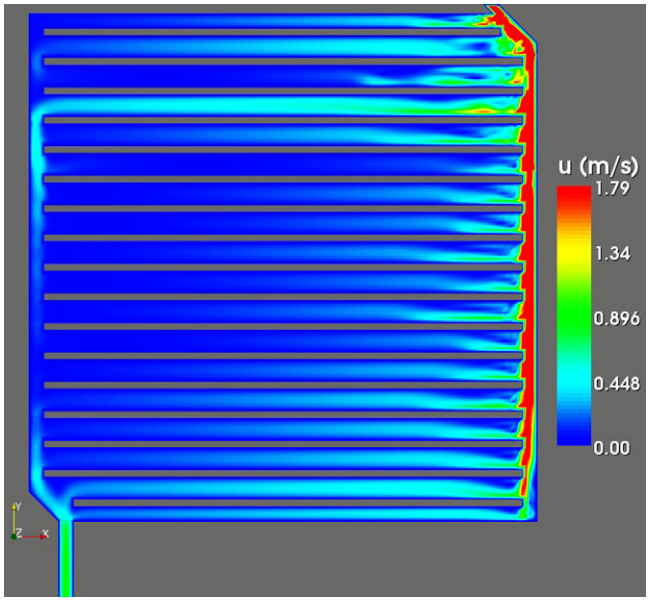

Fig. 11. Velocity magnitude at the middle plane of the channels of the commercial plate.

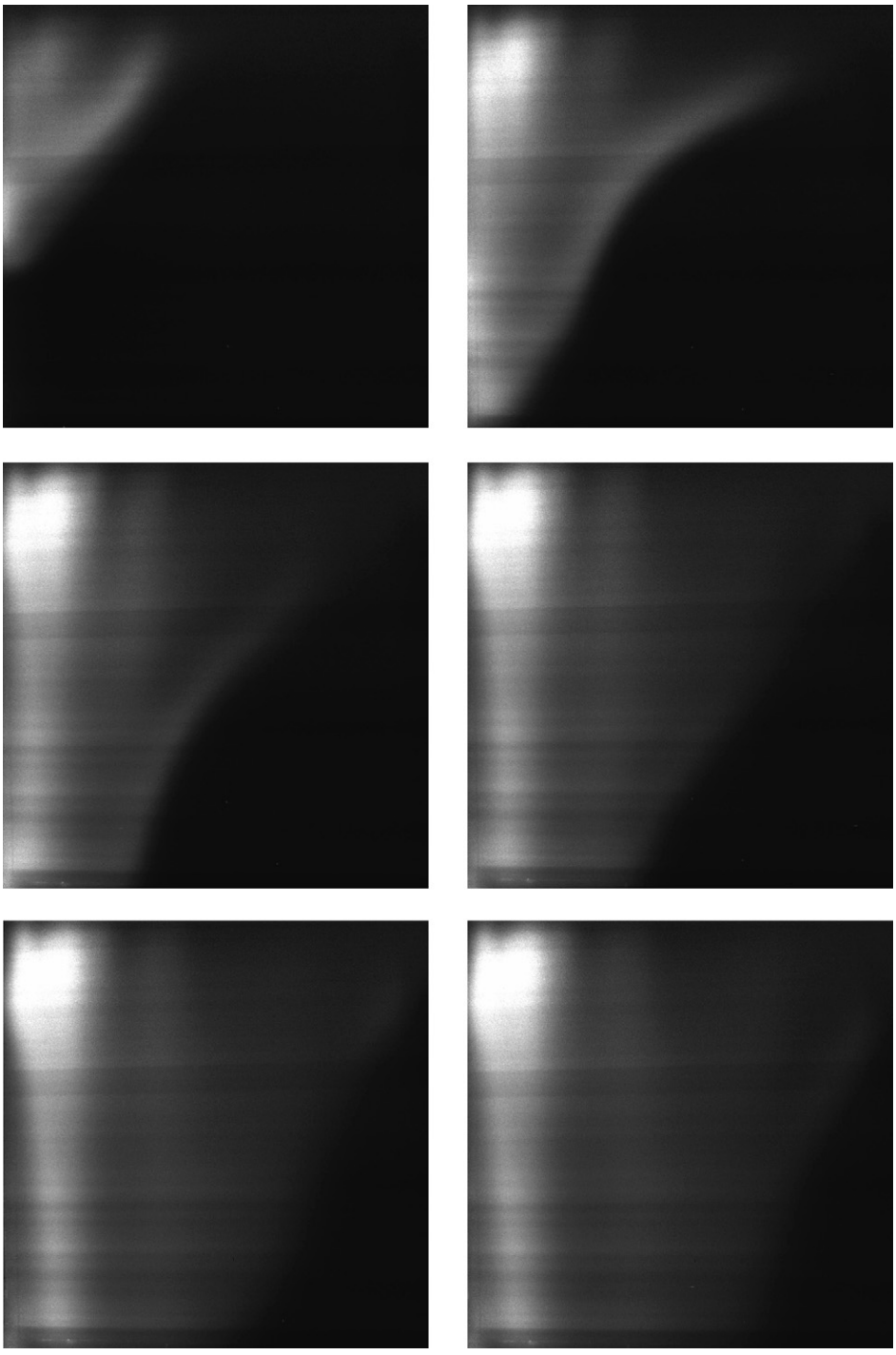

Fig. 12. Flow emerging from the carbon paper in a filling process of the serpentine plate. As in previous figures, images are separated by 0.5 s and flow rate is $1.5\,l\,min^{-1}$.

the diffusion field. As predicted in part I of the study, a strong diffusion near the entrance area is observed, due to the high-pressure values. As time evolves, the gas flow front traversing the GDL very slowly advances covering the whole area, but the resulting distribution is non-uniform, with the air exiting preferentially in the area close to the inlet. The low rate at which the emergent air front advances in the sequence shown in Fig. 12 is explained by the large air volume that exits the GDL near the plate inlet.

From the velocity and pressure distributions determined for the diagonal plate, a deficient diffusion flow distribution can be expected. Fig. 13 presents the results corresponding to this topology. It is quite remarkable to observe how closely the filling pattern follows the pressure distribution. After crossing the backing layer, the flow comes out first from the zones of higher pressure, i.e., from the points where the pressure gradient across the carbon paper is larger. It can be observed that although some air is emerging from the whole

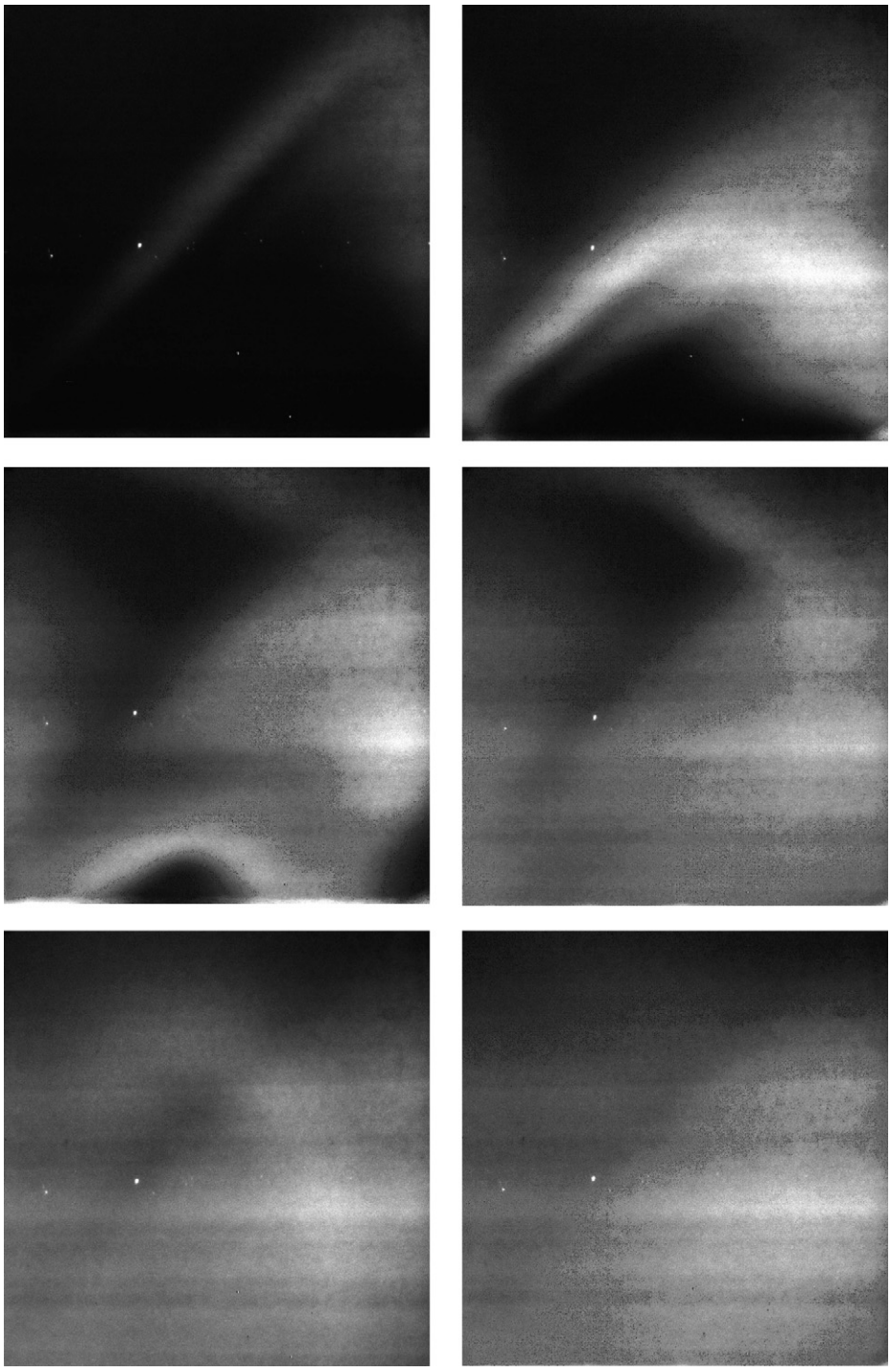

Fig. 13. Filling process of the diagonal plate. As in previous figures, images are separated by 0.5 s and flow rate is 1.5 l min^{-1}.

surface of the bipolar plate, it comes out preferentially from the area comprising the diagonal channels and those below them. A dark band in the zone corresponding to the channels immediately above the diagonal can also be noticed. This non-uniform flow distribution reveals that this particular design is clearly defective and could be easily improved by changing the inlet position or modifying the channel topology. The presence of an area where the flow of acetone-seeded air is very limited will lead to an unbalanced use of the catalyst, and, possibly, to a defective overall efficiency of the fuel cell.

The last topology tested is the one denoted as cascade-type. The results for this plate are depicted in Fig. 14. In this case, the flow emerging from the GDL is very uniform, and very quickly covers the whole layer area. This nice performance is in good agreement with the smooth velocity and pressure distributions measured and calculated in part I of this research, and, in particular, with the roughly

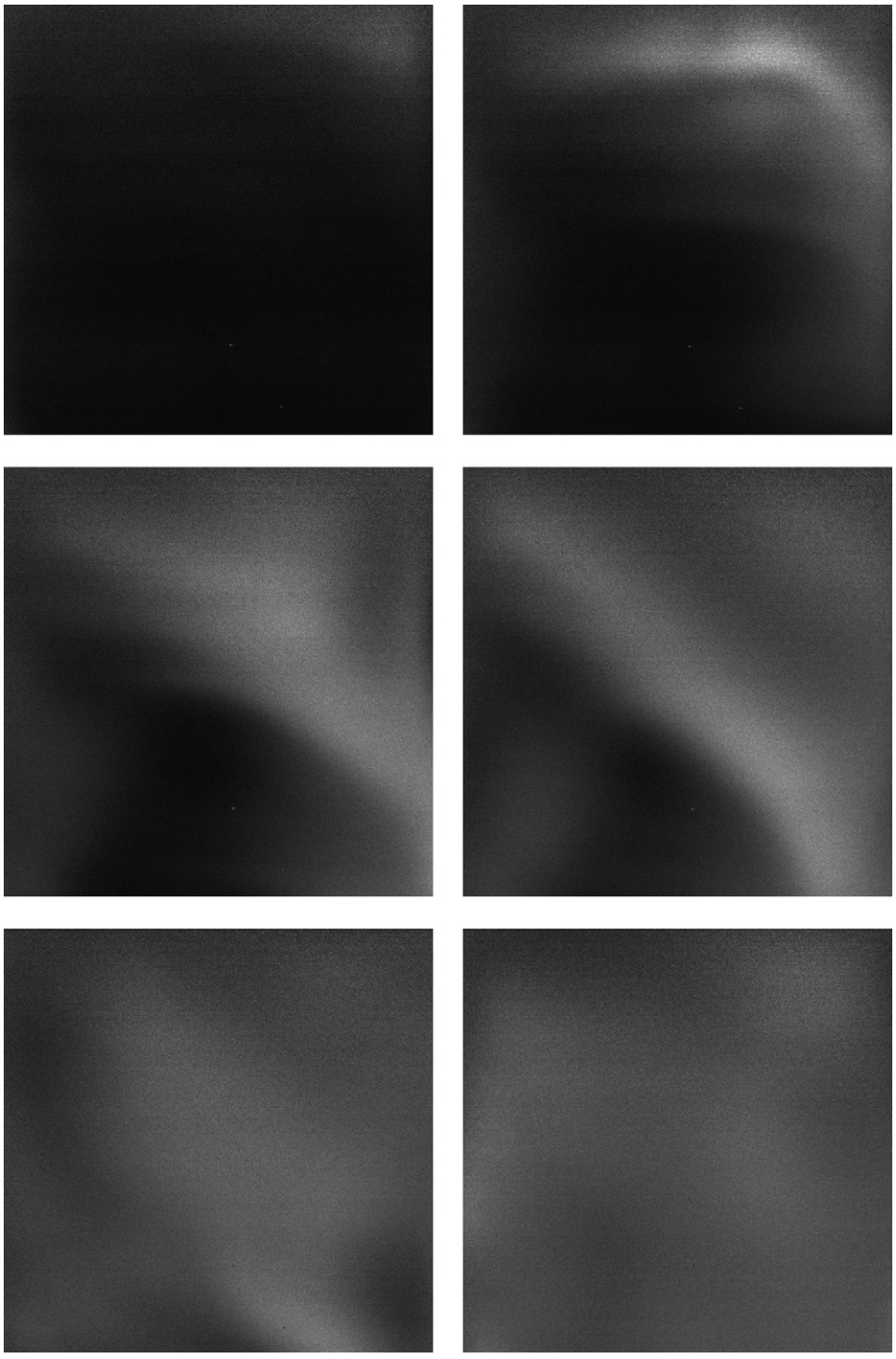

Fig. 14. Filling process of the cascade-type plate. As in previous figures, images are separated by 0.5 s and flow rate is 1.5 l min^{-1}.

constant pressure drop along the different longitudinal channels.

4. Conclusions

An experimental and numerical study has been presented to analyze the gas flow across a GDL from different bipolar plates. It has been shown that the flow through the carbon paper layer is mostly controlled by the pressure gradient across the GDL. Hence, even a non-uniform velocity distribution of the reactant gases in the plate (as visualized with the liquid analogue) can result in a more acceptable distribution over the catalyzed electrode if the pressure field is sufficiently smooth. In the opposite case, a very homogeneous velocity field can yield a defective gas distribution after the GDL, for example if pressure losses are too high. This could be the case for a serpentine type bipolar plate. Thus, special attention should be given to minimize pressure differences among the channels. In the case of the commercial

plate, it is observed that the impinging jet creates a zone of (relative) high pressure at the entrance, which is extended along the right lateral channel and some of the higher channels. This has the effect of a GDL exit velocity significantly greater at the entrance and roughly double at the indicated channels, compared to the values at other zones of the plate. A small effect of the channel ribs is also observed. The cascade plate, especially designed to provide a smooth pressure field results is a very uniform gas flow after the GDL.

In the model employed, the gas flow through the GDL is mainly driven by the pressure gradient, so its distribution is related to the pressure map. Considering that the electrochemical reaction rate increases with the pressure, these maps will be partially indicative of the performance of the cell provided that the reaction rate is uniform over the electrode surface.

Acknowledgements

This research has been partially supported by the Spanish Education and Science Ministry under the project ENE2005-09124-C04-03/ALT, the Aragon Government under the project PM042/2007 and by the Network of Fuel Cell Batteries of the Spanish Council for Scientific Research (CSIC).

References

[1] F. Barreras, A. Lozano, L. Valiño, R. Mustata, C. Marín, J. Power Sources 175 (2008) 841–850.
[2] L. Carrette, K.A. Friedrich, U. Stimming, Fuel Cells 1 (1) (2001) 5–39.
[3] P. Costamagna, S. Srinivasan, J. Power Sources 102 (2001) 253–269.
[4] F. Barreras, A. Lozano, L. Valiño, C. Marín, A. Pascau, J. Power Sources 144 (2005) 54–66.
[5] A. Lozano, F. Barreras, L. Valiño, C. Marín, Exp. Fluids 42 (2) (2007) 301–310.
[6] E. Chen, in: G. Hooger (Ed.), Fuel Cell Technology Handbook, CRC Press, Boca Raton, FL, 2003.
[7] F. Barbir, PEM Fuel Cells: Theory and Practice, Elsevier Academic Press, USA, 2005.
[8] L. Wang, A. Husar, T. Zhou, H. Liu, Int. J. Hydrogen Energy 28 (2003) 1263–1272.
[9] A. Lozano, B. Yip, R.K. Hanson, Exp. Fluids 13 (6) (1992) 369–376.
[10] J.A. Ochoa-Tapia, S. Witaker, Int. J. Heat Mass Transfer 38 (14) (1995) 2635–2646.